



# Quantification of firebrand generation from WUI fuels for model development: Firebrand generation rate, surface temperature and heat release rate

Xiaoyu Ju<sup>a,\*</sup>, Michael Lisano<sup>b</sup>, Mohammadhadi Hajilou<sup>c</sup>, Peter B. Sunderland<sup>d</sup>, Stanislav I. Stoliarov<sup>d</sup>, Lizhong Yang<sup>a</sup>, Michael J. Gollner<sup>e,\*</sup>

<sup>a</sup> State Key Laboratory of Fire Science, University of Science and Technology of China, Hefei, Anhui, China

<sup>b</sup> Department of Electrical Engineering and Computer Sciences, University of California, Berkeley, CA, USA

<sup>c</sup> Shiley School of Engineering, University of Portland, Portland, OR, USA

<sup>d</sup> Department of Fire Protection Engineering, University of Maryland, College Park, MD, USA

<sup>e</sup> Department of Mechanical Engineering, University of California, Berkeley, CA, USA

## ARTICLE INFO

### Keywords:

WUI (Wildland-urban interface)

Firebrands

Temperature

Heat release rate

Numerical modeling

## ABSTRACT

Wildland fires that spread into developed areas, i.e., the wildland-urban interface (WUI), have resulted in numerous disasters over the past few decades, claiming the lives of civilians and causing large-scale property destruction. In these communities, fires often ignite structures by the deposition of small burning embers (firebrand attack) which is unique to these fires and not yet well understood. This study quantifies the in-flight thermal characteristics of firebrands generated by three typical vegetative fuels, namely stone pine, eucalyptus and oak found in the WUI, inside a lab-scale wind tunnel. The effects of fuel characteristics (i.e., species, moisture content and twig diameter) and ambient condition (i.e., crosswind speed) on surface temperature, number generation rate (NGR), and heat release rate ( $HRR_{fb}$ ) were investigated. Firebrand surface temperatures, measured using ratio pyrometry, were insensitive to fuel moisture content and mean twig diameter but higher at higher crosswind speeds. Surface temperature was used to estimate the  $HRR_{fb}$  of each firebrand based on a surface energy balance and compared to overall emissions measurements. While ratio pyrometry best captured firebrand temperatures, infrared video worked well to track firebrands and derive a NGR as a function of time. Correlations were used to organize the NGR,  $HRR_{fb}$ , and mass generation rate (MGR) under different test conditions, and unique correlations were derived for each fuel species. Results showed that the peak NGRs and MGRs for all three fuel species were positively related to crosswind speed but negatively related to fuel moisture content and mean twig diameter. The experimental data, correlations and methods disclosed in this study are important to understand the influence of competing processes on firebrand generation, parameterize fire spread models for time-dependent generation, and improve estimates of downstream ignition potential. Experiments must later be validated against large-scale data before widespread application.

## 1. Introduction

Firebrands are generated when small pieces of smoldering material break off from vegetation or structures during wildland or wildland-urban interface (WUI) fires. These small brands can travel far ahead of the burning fire and deposit on the ground or on structures themselves, igniting components by direct ignition or via a transition from smoldering to flaming. This process presents significant hazards, especially during WUI fires as these resulting “spot fires” can accelerate fire spread

and lead to extensive structure destruction. Nevertheless, firebrand phenomena remain elusive due to the large number of variables and the complex coupling between them [1]. As noted in recent reviews [2–5], generation of firebrands and their ignition of structural fuels have not been well quantified, limiting the ability of models to capture features of real fire spread.

Regarding generation of firebrands, numerous studies have been conducted to investigate the mass and size distributions of firebrands generated by vegetative [6–10] and structural fuels [11,12]. Potential

\* Corresponding authors.

E-mail addresses: [ju.xiaoyu@ustc.edu.cn](mailto:ju.xiaoyu@ustc.edu.cn) (X. Ju), [mgollner@berkeley.edu](mailto:mgollner@berkeley.edu) (M.J. Gollner).

<https://doi.org/10.1016/j.proci.2024.105729>

Received 4 December 2023; Accepted 30 July 2024

Available online 14 August 2024

1540-7489/© 2024 The Combustion Institute. Published by Elsevier Inc. All rights are reserved, including those for text and data mining, AI training, and similar technologies.

issues with these studies is an inability to account for all produced firebrands, as some proportion of firebrands could escape from the ends of the wind tunnel or overhead hood, or land in an area not covered with water-filled pans used to capture firebrands, as well as challenges controlling all potential ambient and fuel variables at large scale. Hajilou et al. [13] developed a small-scale wind tunnel facility (25 cm wide, 20 cm tall, and 61 cm in length), introducing a methodology to account for all firebrands generated from WUI fuels under different environmental conditions while measuring a cumulative firebrand yield from the burning fuels. Following Hajilou's methodology, the current authors [14] developed a larger wind tunnel setup with a longer test section to burn fuels with larger, more complex geometries. The fuel characteristics (i.e., species, dry mass, moisture content, and twig diameter) and ambient condition (i.e., crosswind speed) were varied and correlated to resulting firebrand yields in a comprehensive manner. In addition, the effects of the above factors on mass and size distributions of the collected firebrands were also investigated and quantified.

In addition to the yields and mass and size distributions of firebrands, the generation rates, temperatures, heat release rates ( $HRR_{fb}$ ), smolder time, terminal velocities and surface areas of airborne firebrands generated by real fuels are also desired to improve current fire spread models but are difficult to obtain using current measurement techniques. For example, the firebrand generation rate is an important parameter used to quantify the number and mass generation rate of firebrands (NGR and MGR) by a fuel, rather than just an overall yield. Meanwhile, firebrand surface temperatures may be useful in characterizing the thermal state of a lofted ember [15]. Firebrands with more energy content have been shown to more easily ignite a fuel bed at a shorter time and decrease the critical particle size for downstream ignition [1]. Moreover, if the  $HRR_{fb}$  of a single firebrand could be estimated it would provide an important estimate of the rate at which a firebrand is consumed during transport and thereby the remaining energy available to ignite a recipient fuel [16]. Firebrands with low  $HRR_{fb}$  are more likely to extinguish before igniting a fuel bed. To develop more realistic numerical models of firebrand generation, empirical trends between the above parameters for different WUI fuels under varying ambient conditions should be developed.

This study quantifies the in-flight thermal characteristics of firebrands generated by several vegetative fuels using the same wind tunnel apparatus from our previous work [14], but augmented with new measurements including infrared imagery, ratio pyrometry, and gas sampling. The fuel characteristics and the ambient conditions were

varied over the same conditions from [14], and their effects on the resulting NGRs and MGRs, surface temperatures, and  $HRR_{fb}$  were elucidated. Quantitative relations between these parameters were deduced, which could serve as important inputs when performing future simulations of fire spread in both the wildland and WUI using numerical modeling tools.

## 2. Materials and methods

### 2.1. Experimental setup

The experimental setup in this study is shown in Fig. 1(a), including a wind tunnel, a firebrand collection system and an emission analysis system (indicated by different colored arrows). The wind tunnel is the same as the one in [14], with a test section of 50.0 cm (length)  $\times$  30.5 cm (width)  $\times$  30.5 cm (height). The crosswind speed inside the wind tunnel ( $U_\infty$ ) was set to 1.0 – 4.0 m/s with 1.0 m/s in interval (see Fig. 1(b)) and turbulence intensities were lower than 2 %. Three different fuel species, including the fractal tree branches of stone pine (SP), eucalyptus globulus (EG) and coast live oak (CLO) (see Fig. 1(c)), were ignited at  $U_\infty = 1.0$  m/s inside the wind tunnel by a 5-kW linear burner flame. All the live branches had a length of around 35 cm and dry mass of 50 g. The branches were dried in a convection oven at 90 °C for different lengths of time to obtain branches with different fuel moisture contents (FMC, defined in [14]) between 3 – 44 %. The mean twig diameters of the branches ( $D_{twig}$ ) were 5.0, 8.0 and 11.0 mm, representing the mean values of twig diameter measured using calipers for each branch collected from the base of the branch to the end of each twig. Their uncertainties were within  $\pm 2.0$  mm estimated by the Student's *t*-test with a 95 % confidence interval. The ignition time of a branch exposed to the burner flame was set to the average time for the leaves or needles on the branch to be burnt out at  $U_\infty = 1.0$  m/s for each fuel species. Once the open flame on a branch ceased, the burner flame was extinguished, and the crosswind speed was increased from 1.0 to 2.0, 3.0 or 4.0 m/s for firebrand generation. Such treatment of the branches was used to effectively consume the leaves and fully decompose the twigs to develop correlations for long-distance (smoldering) firebrand spotting predictions. The airborne firebrands in each test were collected and quenched by a water tray at the wind tunnel exit. They were then placed in the foregoing convection oven at 90 °C for at least 24 h to retrieve dry firebrands. The dimension of each dried firebrand was measured for subsequent calculations. The gap between the wind tunnel exit and the

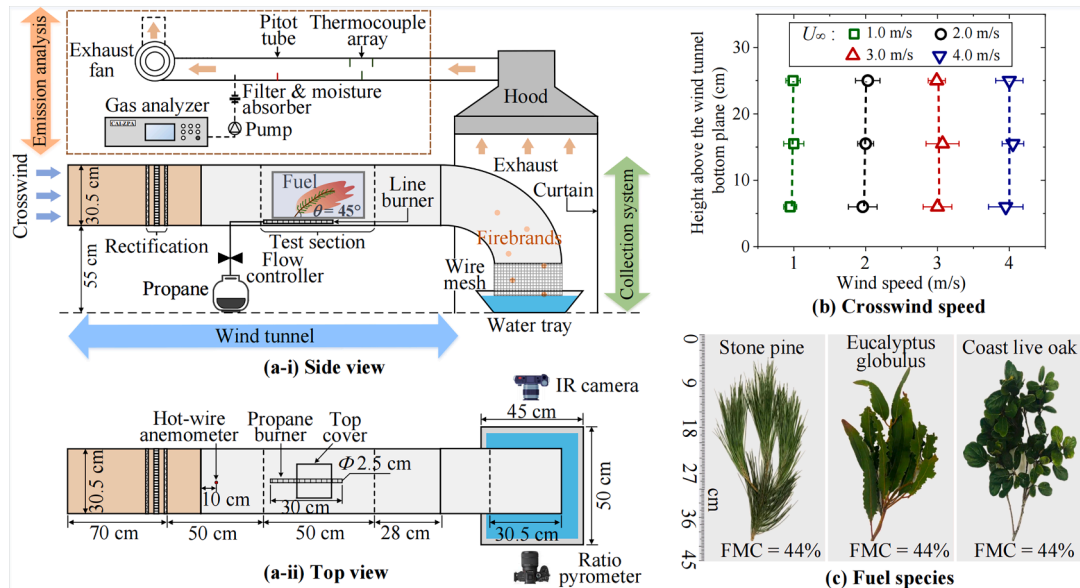


Fig. 1. (a) Experimental setup, (b) crosswind speed inside the wind tunnel and (c) fuel species for firebrand generation.

water tray was enclosed by a layer of wire mesh to keep firebrands from escaping.

The wind tunnel exit was placed under an exhaust hood with a cross-sectional area of  $1.2 \times 1.2 \text{ m}^2$ , the four sides of which were enclosed by fireproof curtains as shown in Fig. 1(a). The gaseous products including  $\text{CO}_2$ ,  $\text{CO}$  and  $\text{O}_2$  emitted/consumed during the burning process were analyzed by a gas analyzer (California Analytical Instruments, ZPA model) to determine the system heat release rates (termed  $\text{HRR}_{\text{system}}$  to distinguish it from  $\text{HRR}_{\text{fb}}$ ). Temperatures and flow velocities of exhaust gases were measured with three K-type thermocouples (their average was used to calculate gas properties) and a pitot flow sensor (VERIS Verabar), respectively. The calibrated flow rates are shown in the Supplementary material (Fig. S1). There were 27 different test conditions for each fuel species and each condition was repeated at least three times.

## 2.2. Firebrand generation rate measurement

A FLIR E60 infrared (IR) thermal camera was placed at the wind tunnel exit to record the firebrand generation process as shown in Fig. 1(a). The camera had a resolution of  $320 \times 240$  pixels, a frame rate of 60 Hz and a temperature measurement range of up to  $650^\circ\text{C}$ . Note that this temperature range was relatively low, saturated, and had a high error due to unknown emissivity values, so IR measurements were only used for tracking each firebrand. The video shot in each test was converted into frames of images and all the images were analyzed frame by frame using a Python code. Each firebrand was tracked as it flew out of the wind tunnel until it entered the water tray and therefore counted as “1”; note that only those that were smoldering and contained zones with temperatures exceeding  $650^\circ\text{C}$  (see Fig. 2) were counted as effective firebrands. The variation of NGR against the elapsed time of a test ( $t_{\text{elapsed}}$ ) could then be calculated by counting all the firebrands in all the images, and the corresponding MGRs were also estimated by multiplying NGR by the mean firebrand mass in each test. Note the mean firebrand mass values vary between different tests.

## 2.3. Ratio pyrometry of firebrand streaks

Ratio pyrometry of firebrand streaks was performed using a color digital camera (Sony DSC-RX10 III) placed at the wind tunnel exit as shown in Fig. 1(a). The camera was the same one used in previous studies [15,17], which was calibrated with a blackbody furnace (Oriol 67,032) at  $600\text{--}1200^\circ\text{C}$ . All images were recorded at  $f = 2.4$ , a focal length of 24 mm, and a distance of 55 cm between the camera and the center plane of the wind tunnel exit. Pyrometry analysis was conducted in Python, with the same methodology documented in [15,17,18]. For each pixel in each image, the normalized pixel value ( $NI_i$ ) was defined as

$$NI_i = \frac{(I_i - I_{i,DC})f^2}{tISO} \quad (1)$$

where  $I_i$  is pixel value,  $i$  denotes R, G or B,  $f$  is f-number,  $t$  is exposure time and  $I_{i,DC}$  is the dark-current pixel value. The pixel values were then converted to temperatures based on the blackbody calibration equation for ratio pyrometry [17],

$$T_{\text{non-null}} = 362.7 \log \left( \frac{NI_G}{NI_R} \right)^3 + 2186.7 \log \left( \frac{NI_G}{NI_R} \right)^2 + 4466.5 \log \frac{NI_G}{NI_R} + 3753.5 \quad (2)$$

where  $T_{\text{non-null}}$  is the non-null temperature at each pixel. The blue pixel values were too low to be useful. Note that pixels approaching saturation (a pixel value of 65,535), pixels with green pixel values below 100 and pixels with raw temperatures outside the calibration range ( $600\text{--}1200^\circ\text{C}$ ) were assigned null temperatures [15]. The uncertainty of  $T_{\text{non-null}}$  at any pixel was estimated to be  $\pm 20^\circ\text{C}$  when the product of the emissivity and transmittance varied by  $\pm 7\%$  between green and red [15,18]. The firebrand streak temperature was further calculated using all the non-null temperatures in each streak as detailed in Section 3.2.

## 3. Results and discussion

### 3.1. Firebrand generation and heat release rate

Fig. 2 shows firebrand transport of a SP branch captured by the IR camera at the wind tunnel exit to calculate real-time NGR (the number of firebrands [pcs] [7] generated per unit time). The branch had a dry mass of 50 g, a fuel moisture content of 16 % and a mean twig diameter of 5.0 mm. As mentioned in Section 2.1, the branch was ignited and burned at a relatively low crosswind speed of 1.0 m/s, which was then ramped up to 4.0 m/s when the open flame on the branch ceased at  $t_{\text{elapsed}} = 140 \text{ s}$  (see Fig. 2(a)). Firebrands were observed to fly out of the wind tunnel exit and enter directly into the water tray (see Fig. 2(b)), extinguishing them. The test would continue until the branch was completely burned out. Note that the firebrand surface temperature measured was much higher than the upper measurement limit of the IR camera ( $650^\circ\text{C}$ ) described in Section 3.2, so temperatures at the limit and above are not accurate. The IR camera was instead used to recognize and track each firebrand, rather than to measure firebrand surface temperature. The video corresponding to Fig. 2 is shown in the Supplementary material.

The system heat release rate contributed by both the branches and firebrands was first analyzed to understand the firebrand generation process. It was calculated via an oxygen consumption calorimetry

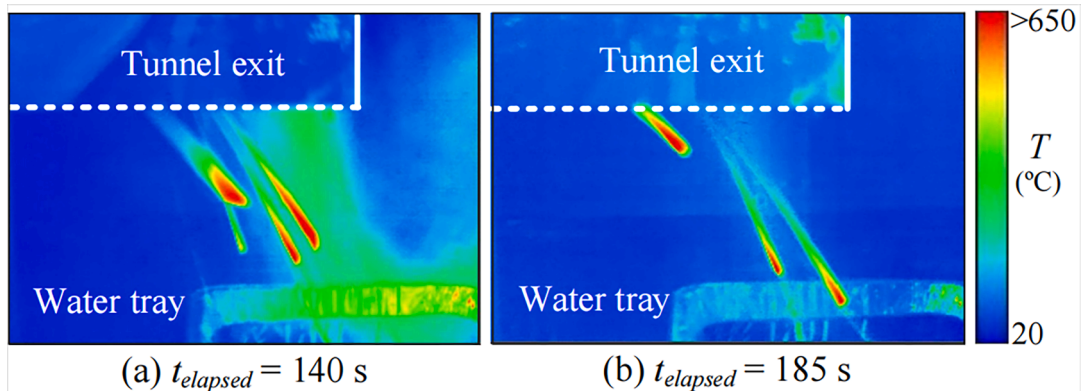


Fig. 2. Firebrand transport phenomena captured by an IR camera to calculate the real-time NGR of an SP branch burning under  $U_\infty = 4.0 \text{ m/s}$ , FMC = 16% and  $D_{\text{twig}} = 5.0 \text{ mm}$ .

method [19], utilizing the measured mass generation/consumption rates of CO<sub>2</sub>, CO and O<sub>2</sub> in each test. Note that the gaseous products emitted/consumed by the burner flame were measured before all the tests and subtracted from the total mass generation/consumption rates of gaseous products. The burner flame was observed to burn in a state of complete combustion. Fig. 3 shows HRR<sub>system</sub> ( $\dot{Q}$ , mean of three repeated tests) of burning SP branches against an elapsed time under the effects of crosswind speed, fuel moisture content and mean twig diameter. The open circle on each curve represents the transition point between flaming and smoldering combustion periods of a branch. It is seen that each curve first peaked in the flaming combustion period and then exhibited a gradual decaying trend in the smoldering combustion period. Additionally, the first peak on the HRR<sub>system</sub> curve (i.e., the peak heat release rate of flaming combustion) is higher for branches with lower fuel moisture content (Fig. 3(b)) and smaller mean twig diameter (Fig. 3(c)) due to more efficient combustion. Corresponding to the HRR<sub>system</sub>, the plots of NGRs ( $f_{fb}$ , with a unit of pcs s<sup>-1</sup>) of SP branches against elapsed time under the effects of the above three factors are shown in Fig. 4, which were extracted from the same firebrand generation tests performed in [14]. Each profile generally exhibits a gradual decaying trend with elapsed time. Meanwhile, the peak NGR was positively related to crosswind speed but negatively related to fuel moisture content and mean twig diameter. This may be because branches are more likely to break to release firebrands under these conditions. Similar results regarding HRR<sub>system</sub> and NGRs were found for EG and CLO branches as shown in the Supplementary material (Figs. S2 and S3).

It should be noted that the dry mass of fuel was fixed in this study (50 g) as it was shown to not affect the overall firebrand yield ( $Y_{firebrand}$ , the ratio of mass of firebrands to total dry mass lost) [14], i.e., the mass of firebrands was linearly related to the total dry mass lost (encompassing both the mass consumed during combustion and converted into firebrands). Then, it is concluded that the mass of firebrands generated per unit time was linearly related to mass loss rate and thus linearly related to HRR<sub>system</sub> (as HRR<sub>system</sub> can be approximated as the product of heat of combustion and mass loss rate of fuel). As a result, the real-time NGR should be related to the corresponding real-time HRR<sub>system</sub> of a branch undergoing smoldering combustion. The variation of real-time NGRs against the corresponding HRR<sub>system</sub> of SP branches is plotted in Fig. 5. It shows that there is a positive relationship between the two terms but the data points under different test conditions deviate from each other. Such deviation was due to the different firebrand yields under different test conditions. Similar results were found for EG and CLO branches as shown in the Supplementary material (Figs. S2 and S3).

Correlation analysis was conducted to connect the above NGR data to HRR<sub>system</sub> data under different test conditions to facilitate model development. For a branch undergoing smoldering combustion, the real-time NGR is a function of the following parameters,

$$f_{fb} \sim (FMC, D_{twig}, \dot{Q}, \rho_{\infty}, c_{p,\infty}, T_{\infty}, U_{\infty}, g) \quad (3)$$

where FMC,  $D_{twig}$  and  $U_{\infty}$  jointly determine the firebrand yield.  $\dot{Q}$ , the

system heat release rate in the smoldering combustion period, is dominated by dry mass of fuel and elapsed time.  $\rho_{\infty}$  (density of ambient air),  $c_{p,\infty}$  (specific heat capacity of air),  $T_{\infty}$  (ambient temperature) and  $g$  (gravitational acceleration) determine the ambient conditions. Therefore, Eq. (3) is rearranged as

$$f_{fb} \sim (Y_{firebrand}, \dot{Q}^*) \quad (4)$$

$Y_{firebrand}$  is related to FMC <sup>$a$</sup>  ( $U_{\infty}/\sqrt{gD_{twig}}$ ) <sup>$b$</sup>  from [14], where  $a$  (<0) and  $b$  (>0) are fitting constants.

$\dot{Q}^*$  is a non-dimensional HRR<sub>system</sub> in the form of  $\dot{Q}^* = \dot{Q}/(\rho_{\infty} c_{p,\infty} T_{\infty} g^{1/2} D_{twig}^{5/2})$ . By separately fitting  $f_{fb}$  with  $Y_{firebrand}$  and  $\dot{Q}^*$ , power-law fitting relationships were found between them, namely  $f_{fb} \sim Y_{firebrand}^{a_1}$  and  $f_{fb} \sim \dot{Q}^{*b_1}$ . The empirical values of the exponents  $a_1$  and  $b_1$  were obtained by the least-squares method of curve fitting. Figs. 6 (a-c) plot the values of  $f_{fb}$  for each fuel species against a combined form of the two terms,  $Y_{firebrand}^{a_1} \dot{Q}^{*b_1}$ . It is found that  $f_{fb}$  has a positive linear correlation with  $Y_{firebrand}^{a_1} \dot{Q}^{*b_1}$  for all three fuel species with a high degree of fit ( $R^2 \geq 0.9674$ ). Additionally, both values of  $a_1$  and  $b_1$  are over 0. This agrees with the observations in Figs. 3 and 4, i.e., the NGR of a fuel species is positively related to HRR<sub>system</sub> and crosswind speed but negatively related to fuel moisture content and mean twig diameter. For numerical modeling tools like FDS (Fire Dynamics Simulator [20]), the HRR<sub>system</sub> of a given fuel can be first calculated as a function of time; therefore, the above empirical correlations could be used to estimate the real-time NGR. In addition, the values of MGR ( $\dot{m}_{fb}$ ) can be computed by multiplying NGR by the mean firebrand mass in each test as shown in Figs. 6(d-f). Furthermore, the above correlations can be classified into two categories to facilitate future WUI fire modeling, which includes conifer (represented by stone pine) and broadleaf (represented by eucalyptus globulus and coast live oak) species. This is because, for long-distance firebrand spotting predictions, the leaves on branches were burnt out and firebrands mainly come from twigs, while the inherent nature of twigs is comparable among similar species common in WUI areas. As a result, the values of  $a_1$  and  $b_1$  could be approximated as 1.4 and 1.0 for conifers, and 0.9 and 1.2 for broadleaf trees. These results must still be verified at larger scales but provide a framework to add time-dependent firebrand generation rates into simulations.

### 3.2. Firebrand surface temperature

Ratio pyrometry was performed on firebrand streaks following the same processing steps proposed in [15,17,18], including assigning null temperatures and smoothing non-null temperatures using  $7 \times 7$  pixel means. Firebrand images were recorded at the wind tunnel exit at 1 Hz. The camera ISO and  $t$  were selected so that the captured images were neither too dim nor too bright, namely the brightest red pixel value was in the range of 20,000–60,000. Fig. 7 presents an image of a SP firebrand

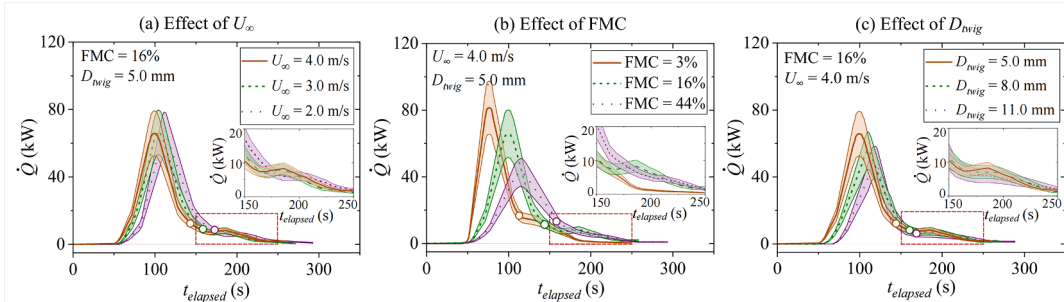


Fig. 3. Heat release rates of burning SP branches vs. elapsed time under the effects of (a) cross wind speed, (b) fuel moisture content, and (c) mean twig diameter. Note that the heat release rate curve on the left side of each open circle corresponds to a flaming combustion period with  $U_{\infty} = 1.0$  m/s.



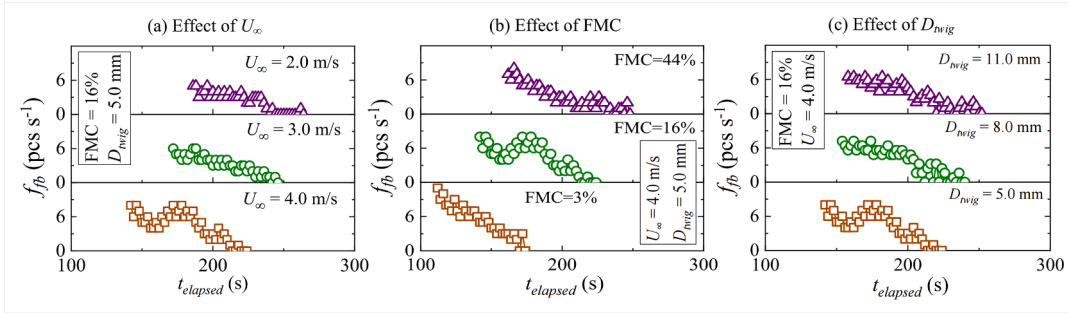


Fig. 4. NGRs in SP branch burning tests vs. elapsed time under the effects of (a) cross wind speed, (b) fuel moisture content and (c) mean twig diameter.

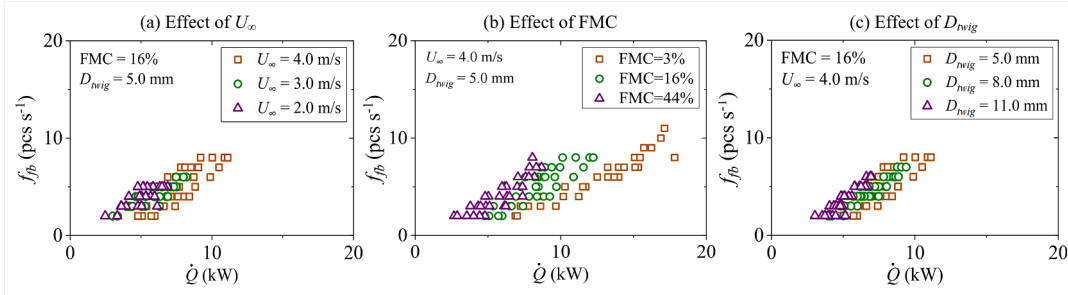


Fig. 5. NGRs in SP branch burning tests vs. corresponding HRR<sub>system</sub> during smoldering combustion periods under the effects of (a) cross wind speed, (b) fuel moisture content and (c) mean twig diameter.

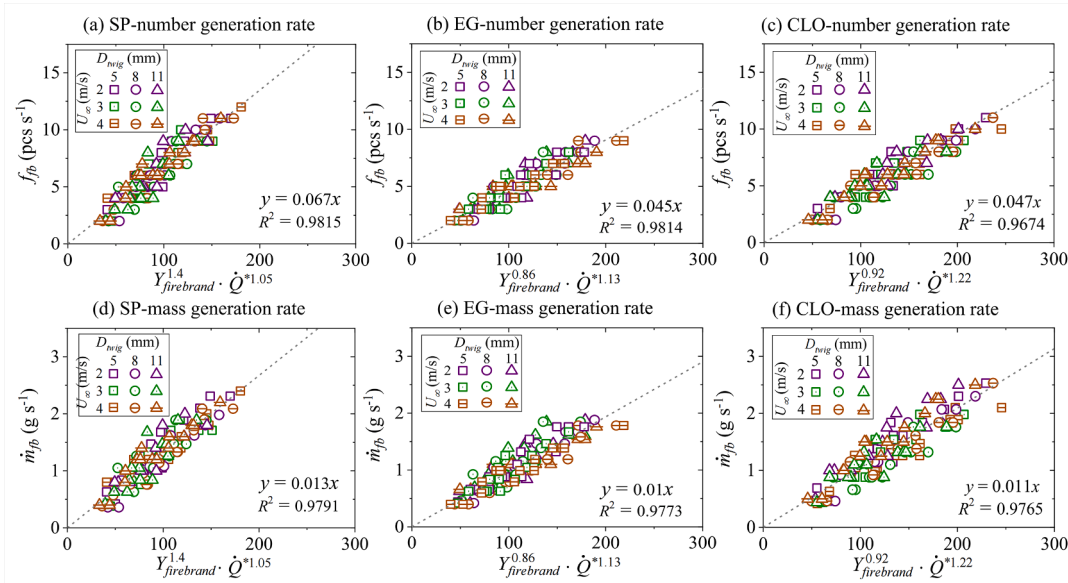


Fig. 6. Correlation analysis of number and mass generation rates of firebrands by all three fuel species under all the test conditions.

streak under the conditions of  $U_\infty = 2.0$  m/s, FMC = 16% and  $D_{twig} = 5.0$  mm, including the original image and the contour plot of the resulting temperatures. The PDF (probability density function) of all the non-null temperatures obtained using ratio pyrometry was also shown. For each firebrand streak, the streak temperature ( $T_{streak}$ ) was defined as the mean of all the non-null temperatures ( $\overline{T_{non-null}}$ ). The mean of all the streak temperatures in each test ( $\overline{T_{streak}}$ ) was defined as the firebrand surface temperature ( $T_{fb}^{surf}$ ) and the standard deviation of the streak temperatures ( $Stdev T_{fb}^{surf}$ ) was also found. Table 1 summarizes all the ratio pyrometry tests performed in this study. It is found that: 1)  $T_{fb}^{surf}$  is

insensitive to fuel moisture content and mean twig diameter but 2) higher under higher crosswind speeds for each fuel species, and 3) for different fuel species,  $T_{fb}^{surf}$  is slightly different from each other. For the observation in 1), it is readily understood that  $T_{fb}^{surf}$  is only related to the inherent properties in the immediate vicinity of a glowing firebrand surface rather than the properties of a branch. By the time glowing combustion is observed, inherent fuel moisture is evaporated from the surface. For 2), the oxygen supply rate was higher under higher crosswind speeds, which could result in a higher firebrand surface temperature due to enhanced pyrolysis reaction rates. This agrees with the results shown in the previous study [15]. Regarding 3), it is related to the

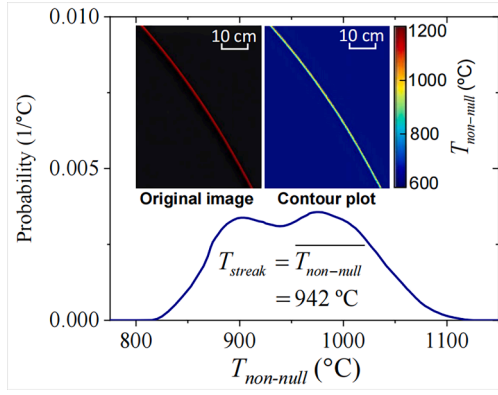


Fig. 7. The original image and the resulting temperature contour plot of a SP firebrand streak, and PDF of all the non-null temperatures obtained using ratio pyrometry. The bin width was 1 °C.

inherent properties of different fuel (wood) species.

### 3.3. Firebrand heat release rate

After calculating the firebrand surface temperature, the  $HRR_{fb}$  of each airborne firebrand was estimated, as it is a key factor affecting downstream ignition. A schematic representation of a cylinder- and disk-shaped firebrand is shown in Fig. 8. The estimation of the  $HRR_{fb}$  of a firebrand was based on the following assumptions: 1) firebrands were idealized as (or equivalent to) cylinders or disks to facilitate the computation of their surface areas. They held their shape while burning in the test window; 2) during the pyrolysis process, the firebrand surface temperature was constant following [21]. Note that all firebrands generated in the same test were assigned the same firebrand surface temperature value (based on the definition of  $T_{fb}^{surf}$  in Section 3.2) for estimation of the corresponding  $HRR_{fb}$ . The  $HRR_{fb}$  data could be further used to estimate the firebrand heat flux to recipient fuels in future modeling work, which is governed by multiple factors including the  $HRR_{fb}$  of a firebrand, heat loss to the environment and heat exchange between the firebrand and recipient fuels [16].

Upon undergoing pyrolysis in a steady state, the firebrand surface temperature is determined by an equilibrium of surface energy including convective and radiative heat losses as well as the heat release due to char oxidation of a firebrand [22],

$$\dot{Q}_{fb} = h_{conv}A(T_{fb}^{surf} - T_{\infty}) + \varepsilon_{fb}\sigma A(T_{fb}^{surf4} - T_{\infty}^4) \quad (5)$$

For a cylinder-shaped firebrand, the surface area  $A = \pi D_{fb}L_{fb}$ , whereas  $A = \pi D_{fb}^2/2$  for a disk-shaped firebrand (which has two sides that exchange heat with its surroundings). For cylinder-shaped firebrands, their diameters ( $D_{fb}$ ) and lengths ( $L_{fb}$ ) were measured individually by a caliper after deposition; for disk-shaped firebrands, their projected areas were determined and the projected region of each

firebrand was equivalent to a circle with the same area and a diameter of  $D_{fb}$ . The heat transfer coefficient,  $h_{conv}$ , was estimated through the Nusselt number,  $Nu = h_{conv}D_{fb}/k_{film}$ , given by the correlation of Kramers [23],

$$Nu = 0.42Pr^{0.2} + 0.57Re^{1/2}Pr^{1/3} \quad (6)$$

where  $k_{film}$  is the thermal conductivity of air at the temperature of  $T_{film} = (T_{fb}^{surf} + T_{\infty})/2$ .  $Pr$  is the Prandtl number and  $Re$  is the Reynolds number, the values of which were estimated by referring to [23,24]. Eq. (6) is valid for  $1 < Re < 10^4$ , where  $Re = vD_{fb}/\nu$  ( $v$  and  $\nu$  are the relative velocity between crosswind and a firebrand obtained by post-processing IR videos, and kinematic viscosity, respectively). The calculated value of  $Re$  was in the range of 53–364 in this work. There is a possible error of

$\pm 2\%$  in  $Nu$  and in  $\sqrt{Re}$  in Eq. (6) as reported by Kramers [23]. The emissivity of the firebrand surface,  $\varepsilon_{fb}$ , was set to 0.9 according to [25]. By solving Eqs. (5) and (6), the  $HRR_{fb}$  of each firebrand,  $\dot{Q}_{fb}$ , could be calculated.

Fig. 9 shows the  $HRR_{fb}$  of single SP firebrands against their projected areas ( $S_{projected}$ ) under the effects of fuel moisture content, crosswind speed, and mean twig diameter; a portion of data points were selectively obscured at regular intervals to enhance clarity for readers. A linear fitting relationship is found between  $\dot{Q}_{fb}$  and  $S_{projected}$  at each test condition. The slope of the fitting line is positively related to crosswind speed but negatively related to fuel moisture content. Meanwhile, it is insensitive to mean twig diameter. Firebrands generated under

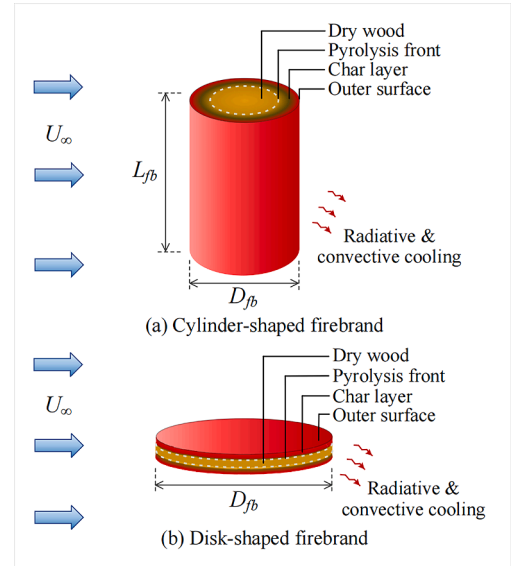


Fig. 8. Schematic representation of a cylinder-shaped (a) and a disk-shaped (b) airborne firebrand undergoing pyrolysis and char oxidation.

Table 1  
Summary of ratio pyrometry tests performed.

Fuel species	Dry mass of fuel (g)	Fuel moisture content (%)	Mean twig diameter (mm)	Crosswind speed (m/s)	No. of firebrand streaks	$T_{fb}^{surf}$ (°C)	Stdev $T_{fb}^{surf}$ (°C)
SP	50	3 %, 16 %, 44 %	5.0, 8.0, 11.0	2.0	936	941	22
				3.0	1114	953	21
				4.0	1409	972	31
				4.0	1240	946	29
EG	50	3 %, 16 %, 44 %	5.0, 8.0, 11.0	2.0	792	920	28
				3.0	1024	932	26
				4.0	1240	946	29
				4.0	1240	946	29
CLO	50	3 %, 16 %, 44 %	5.0, 8.0, 11.0	2.0	828	932	23
				3.0	1252	942	36
				4.0	1467	961	32
				4.0	1467	961	32

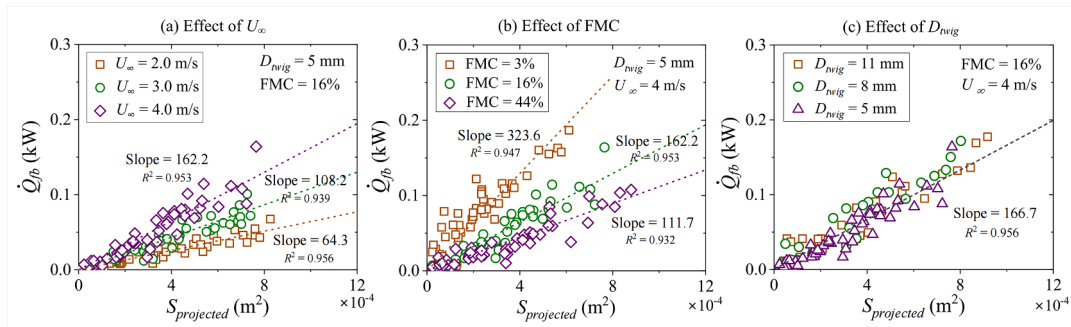


Fig. 9. Heat release rates of single SP firebrands against their projected areas under the effects of fuel moisture content (a), crosswind speed (b), and mean twig diameter (c).

conditions of higher crosswind speed and lower fuel moisture content may have a thicker char layer due to more in-depth pyrolysis, resulting in a higher  $HRR_{fb}$ . In contrast, the twig diameter has little effect on surface pyrolysis if other conditions are held constant; in other words, it does not affect the overall fitting relationship. Similar results were found for EG and CLO firebrands as detailed in the Supplementary material (Figs. S4 and S5). The slopes of the fitting lines between  $\dot{Q}_{fb}$  and  $S_{projected}$  of firebrands under all the test conditions are summarized in Table S1 in the Supplementary material to serve as a database for future tree-scale modeling and validation of firebrand generation.

#### 4. Conclusions

This study quantified firebrand generation from three typical WUI fuels, including stone pine, eucalyptus globulus and coast live oak, inside a lab-scale wind tunnel. The effects of fuel moisture content, crosswind speed, and mean twig diameter on firebrand generation rate, surface temperature and  $HRR_{fb}$  were comprehensively investigated. The peak number generation rate of firebrands was positively correlated to crosswind speed but negatively correlated to fuel moisture content and mean twig diameter. Empirical correlations were first proposed to connect the NGR and MGR of different fuel species under different test conditions to corresponding  $HRR_{system}$  data in the form of  $f_{fb} \sim Y_{firebrand}^{a1} \dot{Q}^{b1}$ . The firebrand surface temperature was measured using ratio pyrometry, which was found to be insensitive to fuel moisture content and mean twig diameter but varied with fuel species and crosswind speed. Utilizing the firebrand surface temperature, the  $HRR_{fb}$  of each firebrand was estimated based on a firebrand surface energy balance. Unique linear fitting correlations were derived between the  $HRR_{fb}$  and projected areas of the firebrands for each fuel species, and the slope of the fitting line was higher at a higher crosswind speed or lower fuel moisture content. However, it was insensitive to mean twig diameter.

This study provides a general method for quantifying the thermal characteristics of firebrands produced by different vegetative fuels and the coupling between fuel heat release rate and resulting firebrand generation. Caution, however, must be taken when applying the correlations provided in this study to other species, at larger scales, or under higher wind speeds. Future experiments should extrapolate and verify these results at full scale under higher crosswind speeds for more species and different materials (e.g. bark and structural fuels). Eventually, this methodology can be embedded in numerical modeling tools to facilitate quantitative wildland or WUI fire spread simulations.

#### Novelty and significance statement

The novelty of this research is that we proposed a general method to quantify the thermal characteristics of firebrands generated by vegetative fuels found in the WUI, including the firebrand generation rate,

surface temperature and heat release rate ( $HRR_{fb}$ ). In particular, the surface temperatures of real airborne firebrands have never been measured and their  $HRR_{fb}$  remain unsolved. Modeling the spread of a fire from vegetation into and within a community has long been a research goal but is hampered by our inability to initialize the generation of firebrands in a controlled and repeatable way. Therefore, the results and methods disclosed in this study could contribute to building an empirical dataset for use to initialize future WUI fire simulations.

#### Author contributions

- XJ: designed and performed research, analyzed data, wrote the paper
- ML: analyzed data, performed research
- MH: designed research, reviewed the paper
- PBS: conceptualization, reviewed the paper
- SIS: supervision, reviewed the paper
- LY: analyzed data, reviewed the paper
- MJG: conceptualization, designed research, reviewed the paper, project administration

#### Declaration of competing interest

The authors declare that they have no known competing financial interests or personal relationships that could have appeared to influence the work reported in this paper.

#### Acknowledgements

This study was supported by the NIST Fire Research Grant Program (60NANB21D122 and 60NANB23D220), UL's Fire Safety Research Institute (FSRI) grant, USTC Research Funds of the Double First-Class Initiative (YD2320002009) and USTC Start Research Funding (KY2320000055). We also thank Mackenzie Conkling and Farouk Mostafa for helping with the experiments.

#### Supplementary materials

Supplementary material associated with this article can be found, in the online version, at [doi:10.1016/j.proci.2024.105729](https://doi.org/10.1016/j.proci.2024.105729).

#### References

- [1] A.C. Fernandez-Pello, Wildland fire spot ignition by sparks and firebrands, *Fire Saf. J.* 91 (2017) 2–10.
- [2] S.L. Manzello, S. Suzuki, M.J. Gollner, A.C. Fernandez-Pello, Role of firebrand combustion in large outdoor fire spread, *Prog. Energy Combust. Sci.* 76 (2020) 100801.
- [3] S.E. Caton, R.S.P. Hakes, D.J. Gorham, A. Zhou, M.J. Gollner, Review of pathways for building fire spread in the wildland urban interface Part I: exposure conditions, *Fire Technol* 53 (2017) 429–473.
- [4] R.S.P. Hakes, S.E. Caton, D.J. Gorham, M.J. Gollner, A review of pathways for building fire spread in the wildland urban interface part II: response of components

- and systems and mitigation strategies in the United States, *Fire Technol* 53 (2017) 475–515.
- [5] A.I. Filkov, V. Tihay-Felicelli, N. Masoudvaziri, D. Rush, A. Valencia, Y. Wang, D. L. Blunck, M.M. Valero, K. Kempna, J. Smolka, J. De Beer, Z. Campbell-Lochrie, F. R. Centeno, M.A. Ibrahim, C.K. Lemmertz, W.C. Tam, A review of thermal exposure and fire spread mechanisms in large outdoor fires and the built environment, *Fire Saf. J.* 140 (2023) 103871.
  - [6] S.L. Manzello, A. Maranghides, W.E. Mell, Firebrand generation from burning vegetation1, *Int. J. Wildland Fire* 16 (2007) 458–462.
  - [7] J.C. Thomas, E.V. Mueller, S. Santamaria, M. Gallagher, M. El Houssami, A. Filkov, K. Clark, N. Skowronski, R.M. Hadden, W. Mell, A. Simeoni, Investigation of firebrand generation from an experimental fire: development of a reliable data collection methodology, *Fire Saf. J.* 91 (2017) 864–871.
  - [8] M. El Houssami, E. Mueller, A. Filkov, J.C. Thomas, N. Skowronski, M.R. Gallagher, K. Clark, R. Kremens, A. Simeoni, Experimental procedures characterising firebrand generation in wildland fires, *Fire Technol* 52 (2016) 731–751.
  - [9] S. Suzuki, S.L. Manzello, Investigating conifer tree combustion in the presence of an applied wind field, *Combust. Science Technol.* 196 (2024) 1168–1185.
  - [10] D.L. Blunck, B. Butler, J. Bailey, N. Wagenbrenner, Multi-scale study of ember production and transport under multiple environmental and fuel conditions, Final Report FSP PROJECT ID (2019) 15. -11.
  - [11] H. Yoshioka, Y. Hayashi, H. Masuda, T. Noguchi, Real-scale fire wind tunnel experiment on generation of firebrands from a house on fire, *Fire Sci. Technol.* 23 (2004) 142–150.
  - [12] S. Suzuki, S.L. Manzello, Y. Hayashi, The size and mass distribution of firebrands collected from ignited building components exposed to wind, *Proc. Combust. Inst.* 34 (2013) 2479–2485.
  - [13] M. Hajilou, S. Hu, T. Roche, P. Garg, M.J. Gollner, A methodology for experimental quantification of firebrand generation from WUI fuels, *Fire Technol* 57 (2021) 2367–2385.
  - [14] X. Ju, M. Conkling, M. Hajilou, S. Lin, F. Mostafa, A. Ayyar, A. McDowell, M. Lisano, M.J. Gollner, Laboratory quantification of firebrand generation from WUI fuels for model development, *Fire Saf. J.* 141 (2023) 103921.
  - [15] J.H. Baldwin, P.B. Sunderland, Ratio pyrometry of emulated firebrand streaks, *Fire Saf. J.* 136 (2023) 103746.
  - [16] Z. Tao, B. Bathras, B. Kwon, B. Biallas, M.J. Gollner, R. Yang, Effect of firebrand size and geometry on heating from a smoldering pile under wind, *Fire Saf. J.* 120 (2021) 103031.
  - [17] J.H. Baldwin, Imaging Pyrometry of Wood Embers Under Simulated Movement, Department of Fire Protection Engineering, University of Maryland, College Park, MD, USA, 2022.
  - [18] D.K. Kim, P.B. Sunderland, Fire ember pyrometry using a color camera, *Fire Saf. J.* 106 (2019) 88–93.
  - [19] J.P. White, E.D. Link, A. Trouvé, P.B. Sunderland, A.W. Marshall, A general calorimetry framework for measurement of combustion efficiency in a suppressed turbulent line fire, *Fire Saf. J.* 92 (2017) 164–176.
  - [20] K.B. McGrattan, H.R. Baum, R.G. Rehm, A. Hamins, G.P. Forney, J.E. Floyd, S. Hostikka, K. Prasad, Fire Dynamics Simulator–Technical Reference Guide, National Institute of Standards and Technology, Building and Fire Research Laboratory, Gaithersburg, 2000.
  - [21] D.T. Stephen, A.C. Fernandez-Pello, On the flight paths of metal particles and embers generated by power lines in high winds—A potential source of wildland fires, *Fire Saf. J.* 30 (1998) 333–356.
  - [22] B.Y. Lattimer, E. Bearinger, S. Wong, J.L. Hodges, Evaluation of models and important parameters for firebrand burning, *Combust. Flame* 235 (2022) 111619.
  - [23] H. Kramers, Heat transfer from spheres to flowing media, *Physica* 12 (1946) 61–80.
  - [24] R.A. Anthenien, S.D. Tse, A.Carlos Fernandez-Pello, On the trajectories of embers initially elevated or lofted by small scale ground fire plumes in high winds, *Fire Saf. J.* 41 (2006) 349–363.
  - [25] K.M. Bryden, K.W. Ragland, C.J. Rutland, Modeling thermally thick pyrolysis of wood, *Biomass Bioenergy* 22 (2002) 41–53.